

Archaean Cratons Record a Duality of Melting Regimes During Early Continental Growth

S. Amrei Ladwig (✉ amrei.ladwig@monash.edu)

Monash University <https://orcid.org/0000-0003-1512-7736>

Priyadarshi Chowdhury

Monash University <https://orcid.org/0000-0001-7544-7331>

Alex J. McCoy-West

Monash University

Oliver Nebel

Monash University

Peter Cawood

Monash University

Article

Keywords: Rare earth elements (REE), Earth, Neoarchaeon

Posted Date: September 22nd, 2020

DOI: <https://doi.org/10.21203/rs.3.rs-53939/v1>

License:  This work is licensed under a Creative Commons Attribution 4.0 International License.

[Read Full License](#)

1 **Archaean cratons record a duality of melting regimes**
2 **during early continental growth**

3

4 S. Amrei Ladwig^{1*}, Priyadarshi Chowdhury¹, Alex J. McCoy-West¹, Oliver Nebel¹, and Peter
5 A. Cawood¹

6

7 ¹School of Earth, Atmosphere and Environment, Monash University, Melbourne, 3800 VIC,
8 Australia

9

10 **Abstract**

11 The tectonic setting and pressure-temperature conditions responsible for the formation of
12 felsic crust on the early Earth remain debated. Rare earth elements (REE) have been extensively
13 used to study the formation of tonalite-trondhjemites-granodiorites (TTGs)- the building
14 blocks of the early felsic crust, but conclusive interpretations based on the chondrite-
15 normalized REE patterns have not materialised because of the inability to distinguish subtle
16 differences. Here we apply a polynomial approach that quantifies the REE patterns by
17 describing their slope and curvature using shaping coefficients to the TTG compositions from
18 five different Archaean cratons. In combination with partial melting modelling, this enables an
19 assessment of the effects of variations in pressure-temperature, degree of melting and residual
20 mineral assemblages on the formation of TTGs. The REE composition of the Archaean TTGs
21 display two distinct trends: (1) a horizontal-trend suggesting their formation in the presence of
22 garnet-poor amphibolitic residues, possibly formed at the base of a thickened crust; and, (2) an
23 inclined-trend consistent with their formation in equilibration with amphibole-poor, but garnet-

24 rich residues at convergent settings (but not necessarily related to plate tectonics). These
25 different melting regimes coexisted during the Paleoarchaeon to Neoarchaeon and provide
26 direct evidence for a duality of petro-tectonic regimes of felsic crust formation on the early
27 Earth.

28 **Main Text**

29 The processes through which felsic continental crust may have formed and evolved on the
30 early Earth remain controversial^{1, 2, 3, 4, 5}. Its record remains preserved in the felsic cores of
31 Archaean cratons that are mainly composed of tonalite–trondhjemite–granodiorite (TTG)
32 suites of granitoids. Consequently, there has been a major impetus in unravelling the formation
33 conditions of TTGs and using them to reconstruct the prevalent tectonic process(es) leading to
34 crustal maturation⁶. Studies show that Archaean TTGs formed via partial melting of
35 metabasalts, however, whether it occurred in presence of the hydrous amphibolite or dry
36 granulite/eclogite residues remains debated^{5, 6, 7, 8, 9, 10, 11, 12, 13}. This has left the interpretations
37 about the role of water in the making of early felsic crust and its tectonic setting(s) ambiguous.
38 Both plate tectonic^{7, 12, 14, 15, 16, 17, 18, 19} and non-plate tectonic (e.g., stagnant-lid) settings^{8, 20, 21,}
39 ^{22, 23, 24, 25, 26, 27, 28} have been suggested for TTG genesis. Alternatively, recent studies suggest
40 that TTG formation may have shifted from stagnant-lid to delamination driven mobile-lid
41 settings during the Archaean^{5, 29, 30, 31, 32}.

42 The trace element compositions of TTGs are controlled by the mineral phases present in
43 the melting residues, which themselves are dependent on the pressure-temperature (P - T)
44 conditions at which metabasalts melt^{6, 8, 10, 33}. For example, TTGs forming at low pressures
45 (LP-TTG; <0.8-1 GPa) show low Sr/Y but high heavy (H)-REE concentrations as plagioclase
46 rich but garnet-absent/poor residues are stable at those conditions, whereas those formed at

47 medium pressures (MP-TTG; ~0.8-1.5 GPa) show higher Sr/Y and lower HREE concentrations
48 as garnet increases and plagioclase decreases in the residues. TTGs forming at even higher
49 pressures (HP-TTG; >1.8-2 GPa) differ from the others by their lower Nb/Ta ratio, which
50 argues for the presence of rutile in their melting residues. These pressure values together with
51 the residual mineralogy have been used to identify the tectonic settings for TTG production
52 like, the formation of MP- to HP-TTGs at great depths in presence of garnet ± rutile rich, dry
53 residues have been preferentially assigned to the melting of mafic crust at subduction zones⁶,
54 ³³. In fact, an onset of subduction driven tectonics during late Archaean has been conjectured
55 based on the increasing abundance of HP-TTGs in the compiled global datasets of TTGs
56 around that time^{5, 18, 34}. However, the compositional variation of TTGs between different
57 cratons within a single time interval remain poorly documented. Such variations, if they exist,
58 will reveal the tectonic variability prevalent at similar times at different locations on the early
59 Earth and will be critical for comprehensively understanding Archaean crust forming
60 processes.

61 Here, we compare the rare earth element (REE) compositions of TTGs from different
62 Archaean cratons, outline the variations between them and discuss their implications for the
63 genesis of the early felsic crust. The investigated cratons include the Pilbara (3.48-2.95 Ga),
64 Kaapvaal (3.46-2.69 Ga), Singhbhum (3.52-3.06 Ga), Yilgarn (2.96-2.60 Ga) and Superior
65 (2.70-2.67 Ga) cratons, which together comprise a significant portion of the preserved
66 Archaean felsic crust. Although there is no strict definition, we have considered all those
67 granitoids as TTGs, which show $\text{SiO}_2 \geq 64$ wt.%, $\text{K}_2\text{O}/\text{Na}_2\text{O} \leq 0.8$, and $\text{Sr}/\text{Y} \geq 10$ ^{5, 6, 33, 34}. The
68 REE data for the Singhbhum craton TTGs are compiled from the published literature, while
69 those for the other cratons are taken from the pre-compiled datasets^{33, 34} (Supplementary Table
70 1a-d). We have also included new analyses from the Yilgarn craton (from GSWA;

71 Supplementary Table 1e). Chondrite normalized REE (REE_N) patterns of TTGs from all the
72 cratons show overlapping patterns (Fig. 1a; Supplementary Fig. 1), which preclude a detailed
73 assessment of trends or systematics within this data. Critical to this approach is that REE as a
74 sum share many geochemical similarities yet possess subtle differences in compatibility
75 between different mineral phases during partial melting and fractional crystallisation. These
76 differences allow distinction between the presence of amphibolite or garnet-rich
77 granulite/eclogite residues during TTG genesis. However, visualisation of these differences
78 and with these unambiguous trends in large datasets cannot be deduced from the classical REE_N
79 illustrations. Our analysis uses a novel method that quantitatively describes the shape of REE_N
80 patterns using a polynomial function³⁵, referred here as the λ -method. This approach reveals
81 subtle differences between the overlapping REE_N patterns of TTGs from different cratons,
82 elucidating unique compositional trends present within them. Further, we seek to reconcile
83 these compositional trends using trace element partitioning modelling and thereby, infer the
84 physical conditions of crust formation for each craton. Our results bear implications for the
85 existence of non-unique regimes of felsic crust formation during the Archaean.

86 **Comparing the TTGs from different cratons**

87 **Approach.** The λ -method involves transforming a REE_N pattern into a polynomial of the
88 form: $\ln([REE]/[REE_N]) = \lambda_0 + \lambda_1 f_1 + \lambda_2 f_2 + \lambda_3 f_3 + \dots + \lambda_n f_n$, where $f_0, f_1, f_2, \dots, f_n$ are
89 orthogonal functions of the ionic radii of REEs and $\lambda_0, \lambda_1, \lambda_2, \dots, \lambda_n$ are the corresponding
90 coefficients³⁵. The λ -coefficients are free from mutual correlation due to the orthogonality of
91 f_n functions and provide specific information about the shape of a REE_N pattern. Thus, they
92 enable quantitative comparison of large sets of REE_N patterns. We have calculated the first
93 three λ -coefficients (λ_0, λ_1 and λ_2) of the REE_N patterns of TTGs (Supplementary Table 1), as

94 together they describe a REE_N pattern with > 95 % accuracy³⁵. λ_0 represents the average REE
95 abundance, whereas λ_1 and λ_2 represent the linear slope and the quadratic curvature of any REE_N
96 pattern, respectively, and both of them can have positive or negative values³⁵. Positive or
97 negative λ_1 values show whether the REE_N pattern is sloping towards the heavy(H) REEs or
98 light(L) REEs; thus, they reflect the relative enrichment and depletion of the LREEs over
99 HREEs, respectively (Fig. 1b). Whereas, $+\lambda_2$ and $-\lambda_2$ values represent whether the curvature of
100 the REE_N pattern is convex or concave, respectively, and effectively show the behaviour of
101 middle(M) REEs relative to LREEs and HREEs (Fig. 1b). Therefore, a plot of λ_1 vs. λ_2 values
102 (hereafter λ -*diagram*) is effective in: (1) understanding the relative control of the slope and
103 curvature in defining REE_N patterns, and (2) identifying the subtle variations among larger
104 REE datasets. Here we have considered only those samples that have ≥ 10 measured REE
105 concentrations so that the results remain statistically robust³⁵.

106 **Compositional trends of the TTGs in λ -diagram.** Figure 2(a-e) shows the distribution
107 of the REE_N patterns of TTGs in a λ -diagram for each craton. Superimposed on the plot of
108 individual data points are the 2D fields of kernel density estimation by the TTGs from each
109 craton. We have also plotted the kernel density estimation of λ_1 and λ_2 individually to show
110 their variation between each craton. The plots show that TTGs of each craton occupy a distinct
111 domain in λ -diagrams despite showing considerable variation in their individual λ_1 and λ_2
112 values. However, the domains of different cratons show some overlap due to their comparable
113 range of either λ_1 or λ_2 values. For instance, the TTGs of Pilbara, Kaapvaal and Singhbhum
114 cratons (Fig. 2a-b, d) exhibit λ_1 values varying between +10 to +25 whereas those of Yilgarn
115 and Superior cratons (Fig. 2c, e) show a slightly higher range of λ_1 values (+15 to +30). This
116 suggests that TTGs from the latter two cratons are slightly more enriched in LREEs.
117 Differences between the TTGs from different cratons are more profound in their λ_2 values. The

118 TTGs from Pilbara, Singhbhum and Yilgarn cratons (Fig. 2a-c) show restricted ranges of λ_2
119 values centred around +40 to +60 as shown by their sharp kernel density peaks, whereas those
120 from the Kaapvaal and Superior cratons (Fig. 2d-e) define a broader range of λ_2 values as shown
121 by their wide kernel density peaks spread-out over +80 to +10 and +50 to -30, respectively.
122 This suggests that the TTGs of Pilbara, Singhbhum and Yilgarn cratons predominantly show
123 MREE-depleted REE_N patterns (high $+\lambda_2$), whereas the TTGs of Kaapvaal craton show REE_N
124 patterns characterized by varying degree of MREE depletion. The TTGs of the Superior craton
125 show both $+\lambda_2$ and $-\lambda_2$ values (Fig. 2e), which argue for the presence of MREE depleted as
126 well as enriched TTGs.

127 The different co-variation of λ_1 and λ_2 coefficients results in unique distributions for the
128 TTGs of each craton, which can be classified as a ‘horizontal-trend’ or an ‘inclined-trend’
129 based on their shape. The horizontal-trend shows greater variability in λ_1 than λ_2 values as
130 observed for the TTGs of Pilbara, Singhbhum or Yilgarn cratons (Fig. 2a-c). This trend implies
131 that the REE_N patterns of the TTGs vary mostly in the extent of LREE enrichment, whereas
132 they show comparable MREE depletion. The inclined-trend, as shown by the TTGs of
133 Kaapvaal and Superior cratons, indicates a negative correlation between λ_1 and λ_2 values (Fig.
134 2d-e). This implies that a continuous range of TTG compositions exists, with a progressive and
135 concomitant enrichment of LREEs and MREEs. While TTGs of both Kaapvaal and Superior
136 cratons exhibit this trend, it is considerably more pronounced for the latter.

137 **Compositional trend of the combined dataset.** The REE_N patterns of TTGs from all the
138 five cratons show an inclined-trend when plotted together in λ -diagram (Fig. 2f). Here, we have
139 considered only those TTGs whose radiometric crystallisation ages are known (Supplementary
140 Table 1). Clearly, the Neoproterozoic TTGs of Superior craton control this observed inclined-
141 trend (cf. Figs. 2e & 2f). However, the overall distribution suggests that TTGs became

142 progressively enriched in MREEs relative to LREEs-HREEs (from convex to concave) as the
 143 Earth progressed from Paleo-Mesoarchaeon to Neoarchaeon. Notably, the horizontal-trend
 144 shown by the TTGs of Pilbara, Singhbhum and Yilgarn cratons cannot be observed in this plot.
 145 This is because the Superior and Kaapvaal TTGs dominate the combined dataset ($n = 285$ of
 146 401) and thus, control its trend. Moreover, the horizontal- and inclined-trends for the individual
 147 cratons are controlled by the variations in their λ_2 values as all of them show a similar range of
 148 λ_1 values. Consequently, the trend within the larger, combined dataset is controlled by the
 149 spread of λ_2 values. This shows how regional variability can get masked and hide the natural
 150 complexity in large global compilations.

151 **Petrogenetic controls on the λ -diagram trends**

152 Considering that TTGs mainly form via partial melting^{5, 6}, we model the trace-element
 153 partitioning between TTG-type felsic melt and residual assemblage during melting to
 154 underscore the physical parameters that control the observed REE trends of TTGs in the λ -
 155 diagram. We use the equation for batch melting in a closed system:

$$156 \quad C_{TTG} = \frac{C_s}{(1 - F)D^{r/TTG} + F}, \text{ where } D^{r/TTG} \left(= \sum_j K_d^{j/TTG} X_j \right)$$

157 The terms $C, F, D^{r/TTG}, K_d^{j/TTG}$ & X represent the REE concentration, melt-fraction, bulk
 158 distribution coefficient, partitioning coefficient, and modal proportions of phases in the
 159 residual assemblage, respectively. The sub-/superscripts: TTG, s, r & j represent the TTG-melt,
 160 source rock, residual assemblage, and residual phases, respectively. The predicted REE
 161 compositions of different TTG melt-fractions, present in equilibrium with different residual
 162 assemblages, are then transformed into their λ -coefficients and compared against those of the

163 natural TTGs. As our initial source rock composition, we have used the average composition
164 of the enriched Archaean tholeiites (EAT³⁶). This is consistent with the recent findings that
165 enriched tholeiitic basalts are probably the most suitable source rocks for TTGs^{8, 37, 38}. For
166 computing the $D^{r/TTG}$, we have used the K_d values of Bédard²⁰ (Supplementary Table 2)
167 whereas the necessary information about the residual assemblages (mineral phases and their
168 proportion) present in equilibrium with various TTG melt-fractions are taken from a recently
169 published phase equilibria model computed for the average EAT composition³⁹
170 (Supplementary Table 3). We have calculated the REE composition for the melt-fractions
171 varying between ~5-40 % and are present with different residual assemblages along three
172 different geotherms of 500, 750 and 1000 °C/GPa (Supplementary Tab 4).

173 Figure 3 shows the REE compositions of these modelled melts in the λ -diagram (also see
174 Supplementary Fig. 2-4). The melt compositions vary between the geotherms along which
175 partial melting is modelled. In particular, the composition of a given melt-fraction shifts to
176 lower λ_2 values as the geotherm gets colder. This is because different geotherms alter the
177 residual assemblages, particularly the proportion of different residual minerals for any given
178 melt-fraction. This affects the $D^{r/TTG}$ and thereby, the composition of the given melt-fraction.
179 For example, at a fixed melt fraction of 20 % the proportion of garnet in the residue increases
180 from ~5 %, to ~27 %, and then to ~39 % as the apparent geotherm decreases from 1000 to 750
181 and 500°C/GPa, respectively). This shifts the modelled melt compositions to higher $+\lambda_1$ values
182 with decreasing geotherms since garnet preferentially sequesters HREEs over LREEs²⁰.
183 Similarly, at a melt-fraction of 20 % the proportion of amphibole decreases from ~30 % to
184 ~21 % and 16 % as the apparent geotherm decreases from 1000 to 500°C/GPa. This decreases
185 the λ_2 values of modelled melt compositions since amphibole, particularly the

186 (magnesian-)hornblende to pargasitic compositions that are mainly present in metabasalts,
187 preferentially incorporates the MREEs over LREEs or HREEs in their structure^{40, 41, 42}.

188 Furthermore, the modelled melt compositions evolve similarly in λ -diagrams as a function
189 of the melt-fraction for all the geotherms. For example, if the melt-fractions formed along the
190 750°C/GPa geotherm are considered, we see that the melt composition evolves towards higher
191 λ_1 and lower λ_2 values as the melt-fraction increases from ~5 % to ~35 %. This defines a linear
192 trend with negative slope in the λ -diagram. This evolution in melt composition is controlled by
193 the increasing proportions of garnet + clinopyroxene, and the decreasing proportion of
194 amphibole in the residue (Fig. 3). Once the amphibole gets exhausted from the residue ($F \approx$
195 35 %), the melt composition takes a leftward hook on the λ -diagram heading towards lower λ_1
196 values upon further melting but without any significant change in λ_2 values (Fig. 3). This is
197 controlled by the declining proportions of garnet and plagioclase in the residue (Fig. 3). The
198 overall evolution of the melt composition thus, defines a ‘tilted-J’ shaped trend in the λ -
199 diagram. The lower melt-fractions corresponding to the limb of this trend ($\lambda_1 = +16$ to $+27$; λ_2
200 $= +150$ to -10) represent melting with an amphibolitic residue, whose amphibole/garnet ratio
201 decreases as the partial melting progresses. In contrast, the higher melt-fractions corresponding
202 to the hook-shaped bend ($\lambda_1 = +25$ to $+21$; $\lambda_2 = -20$ to -33) represent melting in equilibrium
203 with an amphibole-free, garnet-pyroxene granulitic residue (cf. Fig. 3a-b). Our models further
204 show that melts with amphibolitic residue show higher λ_2 values as compared to the melt
205 equilibrating with amphibole-free granulites ($\Delta\lambda_2 = >100$), whereas the corresponding λ_1
206 values remain comparable ($\Delta\lambda_1 = <10$).

207 Overall, the modelled melt compositions computed along the ~750 and 1000°C/GPa
208 geotherms encompass the majority (≥ 60 %) of the natural TTG compositions from each of the
209 studied cratons in the λ -diagrams (Fig. 3). The TTGs of the Yilgarn craton, also show some

210 agreement with melt compositions formed at cooler geotherms (down to 500°C/GPa). To
211 evaluate the effect of variable source rock composition, we have further modelled the melt
212 compositions derived from the melting of depleted Archaean tholeiites (DAT³⁶) and Coucal
213 basalts⁸- variants of enriched Archaean basalts (Supplementary Figs. 2-4). Overall, the melts
214 produced from EAT or Coucal basalts along hotter (>700-1100°C/GPa) geotherms resemble
215 the natural TTG compositions better than the melts obtained from DAT except for the Superior
216 Province TTGs (cf. Supplementary Figs. 2-4).

217 **Discussion and Implications**

218 Our results highlight that: (1) each craton has a distinctive REE composition that emerges
219 when applying the λ -method, and (2) globally, these REE patterns can be grouped into two
220 variants, implying that cratons show a duality in the Archaean crust forming processes (Fig.
221 2). The trace element modelling further shows that these compositional trends are controlled
222 by the petrogenetic factors, namely the P - T conditions and the geotherm at which TTG melts
223 form from a given metabasaltic source.

224 **Factors controlling the compositional trends.** TTGs defining the ‘horizontal-trends’
225 show a greater spread in λ_1 values than in λ_2 values (Figs. 2-3), which suggests that they have
226 a wider range of relative LREE-enrichment for a consistent amount of MREE depletion relative
227 to the other REE. Trace element modelling shows that partial melting of enriched metabasalts
228 along different geotherms of > 700-1000°C/GPa can reproduce this spread of $+\lambda_1$ -values of the
229 TTGs as garnet proportion in the residue increases with colder geotherms, which in turn
230 increases the preferential sequestration of HREEs over LREEs. Besides variable geotherms of
231 melting, intrinsic variations in the original mafic source rock compositions would also lead to
232 variably enriched TTG-melt compositions. Given that Archaean metabasalts show variable

233 LREE-enrichment^{5, 36}, it is logical that such variability would have been transferred into the
234 TTG compositions. Thus, variations in source rock compositions and geotherms of partial
235 melting likely cause the TTG compositions to define a horizontal trend in λ -diagram, as
236 observed in cases of Pilbara, Singhbhum and Yilgarn cratons. On the other hand, the consistent
237 but high $+\lambda_2$ -values (+30 to +100) shown by the TTGs of these cratons is caused by the presence
238 of amphibole in the residue, which preferentially retains the MREEs. Our trace element
239 modelling confirms this, and suggests that TTGs of Pilbara, Singhbhum and Yilgarn cratons
240 correspond to a melt-fraction of ~20-25 % that had equilibrated with amphibolitic residues
241 having variable proportions of garnet.

242 In contrast, the ‘inclined-trends’ can be reproduced by forming TTGs in presence of a
243 residual assemblage that is progressively becoming depleted in amphibole and enriched in
244 garnet. The continuous exhaustion of amphibole during melting produces melts enriched in
245 MREEs, which eventually flips the curvature of the REE_N pattern from convex to concave. The
246 increasing proportion of garnet preferentially retains the HREE in the residue and enhances the
247 relative enrichment of LREEs over the HREEs in the melt. This explains the increase in the
248 slope of the REE_N patterns. Therefore, the inclined-trends shown by the TTGs of Kaapvaal
249 craton and Superior Province are controlled by the decreasing amphibole-to-garnet ratio,
250 reflecting progressive melting at greater depths along a restricted range of geotherms. The high
251 $+\lambda_2$ (and low- λ_1) end of an inclined-trend represents lower melt-fractions equilibrating with
252 garnet-poor amphibolite residues, whereas the low- λ_2 (and high- λ_1) end represents higher melt-
253 fractions equilibrating with amphibole-poor/absent, garnet granulite (garnet + pyroxene +
254 plagioclase) residues.

255 Thus, the results show that TTGs formed at variable P - T conditions in presence of different
256 residual assemblages throughout the Archaean. While the TTGs in equilibrium with

257 amphibole-free, garnet granulites commonly suggest melting at higher pressures, TTGs
258 derived from garnet-amphibolites suggest melting at relatively lower pressure conditions^{8, 9, 10,}
259 ^{11, 39}.

260 **Implications.** This study shows that TTG formation occurred in the presence of both
261 hydrous amphibolite and dry granulites during the Archaean. The melting of metabasalts starts
262 with a garnet-absent amphibolite (amphibole + plagioclase) assemblage and progresses into
263 garnet-bearing amphibolite with increasing melt-fraction. The dehydration breakdown of
264 amphibole dominates the TTG production during this stage as evident from the decreasing
265 proportion of amphibole. REE composition of the TTGs from Pilbara, Singhbhum and Yilgarn
266 cratons represent this regime of mafic crustal melting. However, both amphibole and
267 plagioclase are not completely exhausted from the residues of these TTGs. Whereas for the
268 Kaapvaal craton and Superior province, melting started from amphibolites but progressed to a
269 stage such that amphibole-absent, garnet-rich anhydrous assemblages (garnet + pyroxene +
270 plagioclase) may have melted to produce TTGs. In terms of the TTG classification, the
271 amphibolite assemblages yielded LP- to MP-TTG depending upon the garnet content, whereas
272 amphibole-poor/absent granulite residues correspond to MP to HP-TTGs⁶. It must be noted
273 that HP-TTGs primarily differ from MP-TTGs in Nb/Ta ratios. Given that λ -diagrams do not
274 include Nb or Ta, it is not straightforward to distinguish between MP-TTGs and HP-TTGs
275 using this method. Furthermore, the presence of amphibole-equilibrated TTGs in all the cratons
276 strongly argue that hydrated mafic crust was prevalent during the Archaean, which underscores
277 the presence and importance of water in the making of the early felsic crust.

278 Our results also bear implications for the tectonic setting(s) where early felsic crust may
279 have formed. The TTGs of the Pilbara, Singhbhum and Yilgarn cratons, defining the
280 horizontal-trend in λ -diagram, dominantly formed at relatively, lower pressures (~0.9-1.2 GPa)

281 along the geotherms of $\sim 750\text{-}1000^\circ\text{C/GPa}$ (Fig. 3). These pressure values correspond to the
282 depths of $\sim 25\text{-}35$ km (for an average crustal density of $\sim 2850\text{-}2900$ kg/m³ considering the mafic
283 nature of Archaean crust), which fall around the maximum thickness estimates of Earth's early
284 mafic crust⁴³. Such physical conditions of melting can easily be attained at the base of plateau-
285 like, thick mafic crust^{8, 20, 24, 25, 44, 45, 46} (Fig. 4a) under the inferred hotter mantle conditions of
286 the Archaean⁴³. This tectonic interpretation is consistent with those of the previous studies on
287 Singhbhum and Pilbara cratons^{8, 47}. Even for the Yilgarn craton, a recent study suggested
288 formation of Neoarchaean higher pressure TTGs at the base of a thickened crust²⁷. In contrast,
289 TTGs defining an inclined-trend, as seen for the Kaapvaal craton and Superior province imply
290 melting at pressures ranging from $\sim 0.9\text{-}1.6$ GPa but along similar geotherms of $\sim 750\text{-}$
291 1000°C/GPa (Fig. 3), which corresponds to a depth range of $\sim 25\text{-}45$ km. Melting at
292 depths $>35\text{-}45$ km requires either an exceptionally thick primary crust, or the presence of some
293 convergent tectonics that can bury the mafic crust to those depths. Although cannot be ruled
294 out, a widespread presence of $>35\text{-}40$ km thick mafic crust lacks strong geological support^{48,}
295 ⁴⁹. On the contrary, isolated events of hotter subduction^{6, 7, 29, 50} and lithospheric peeling driven
296 convergent tectonics^{29, 31, 32} have been invoked to occur under the Archaean mantle conditions.
297 These convergent settings provide sites where the melting of mafic crust can occur at both
298 shallow and deeper levels (Fig. 4b). However, we emphasise that these convergent processes
299 do not necessarily equate to a globally linked system of plate tectonics^{30, 51}. Therefore, this
300 study highlights that a dual regime of felsic crust formation during the Archaean, in terms of
301 the depth and temperature of melting, likely corresponds to a duality of the tectonic settings⁵².
302 We, therefore, caution that studying a single craton or even pluton cannot fully document the
303 wide spectrum of Archaean geodynamic environments.

304 **Acknowledgements**

305 We thank Jean-François Moyen and Tim Ivanic for providing Archaean TTG datasets as
306 well as their openness to discussion. This research was supported by ARC grant FL160100168
307 to Peter Cawood.

308 **Author contributions**

309 A.L. and P.C. developed the melting model and generated the code on Matlab, with
310 petrologic input from A.M.W. A.L., P.C., and A.M.W. wrote the manuscript, with all authors
311 contributing to discussions and finessing the work.

312 **References**

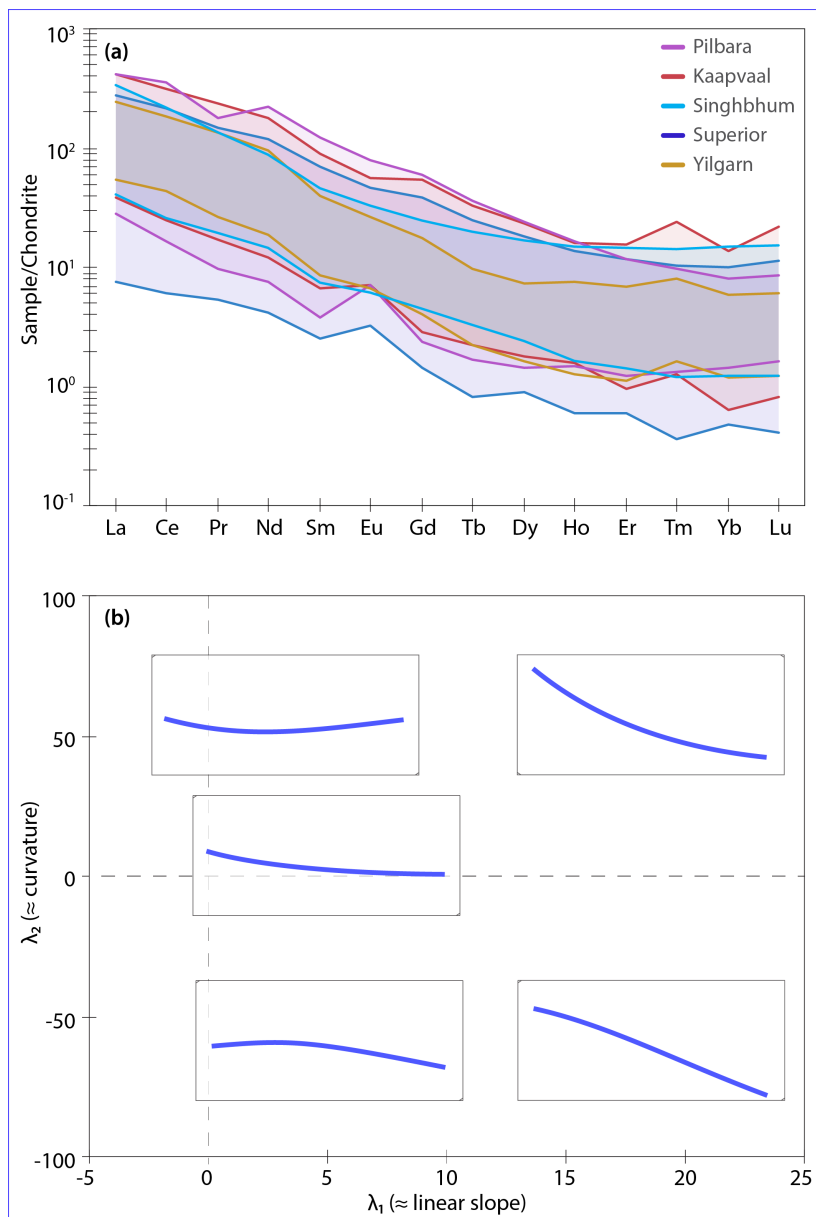
- 313 1. Cawood PA, Hawkesworth CJ, Dhuime B. The continental record and the generation
314 of continental crust. *Geol Soc Am Bull* 2013, **125**(1-2): 14-32.
315
- 316 2. Condie K, Pease V. When Did Plate Tectonics Begin on Planet Earth? *Geological*
317 *Society of America* 2008.
318
- 319 3. Korenaga J. Crustal evolution and mantle dynamics through Earth history. *Philos T R*
320 *Soc A* 2018, **376**(2132).
321
- 322 4. McCoy-West AJ, Chowdhury P, Burton KW, Sossi P, Nowell GM, Fitton JG, *et al.*
323 Extensive crustal extraction in Earth's early history inferred from molybdenum
324 isotopes. *Nat Geosci* 2019, **12**(11): 946-+.
325
- 326 5. Moyen JF, Laurent O. Archaean tectonic systems: A view from igneous rocks. *Lithos*
327 2018, **302**: 99-125.
328
- 329 6. Moyen JF, Martin H. Forty years of TTG research. *Lithos* 2012, **148**: 312-336.
330
- 331 7. Foley SF, Buhre S, Jacob DE. Evolution of the Archaean crust by delamination and
332 shallow subduction. *Nature* 2003, **421**(6920): 249-252.
333
- 334 8. Johnson TE, Brown M, Gardiner NJ, Kirkland CL, Smithies RH. Earth's first stable
335 continents did not form by subduction (vol 543, pg 239, 2017). *Nature* 2017,
336 **543**(7644): 510-510.
337
- 338 9. Moyen JF, Stevens G. Experimental Constraints on TTG Petrogenesis: Implications for
339 Archean Geodynamics. In: (AGU) AGU (ed). *Archean Geodynamics and*
340 *Environments*, 2006, pp 149–175.
341
- 342 10. Palin RM, White RW, Green ECR. Partial melting of metabasic rocks and the
343 generation of tonalitic-trondhjemitic-granodioritic (TTG) crust in the Archaean:
344 Constraints from phase equilibrium modelling. *Precambrian Research* 2016, **287**: 73-
345 90.
346
- 347 11. Qian Q, Hermann J. Partial melting of lower crust at 10-15 kbar: constraints on adakite
348 and TTG formation. *Contrib Mineral Petr* 2013, **165**(6): 1195-1224.

- 349
- 350 12. Rapp RP, Shimizu N, Norman MD. Growth of early continental crust by partial melting
351 of eclogite. *Nature* 2003, **425**(6958): 605-609.
- 352
- 353 13. Xiong X-L. Trace element evidence for growth of early continental crust by melting of
354 rutile-bearing hydrous eclogite. *Geology* 2006, **34**(11): 945-948.
- 355
- 356 14. Hoffmann JE, Nagel TJ, Munker C, Naeraa T, Rosing MT. Constraining the process of
357 Eoarchean TTG formation in the Itsaq Gneiss Complex, southern West Greenland.
358 *Earth and Planetary Science Letters* 2014, **388**: 374-386.
- 359
- 360 15. Hopkins M, Harrison TM, Manning CE. Low heat flow inferred from > 4 Gyr zircons
361 suggests Hadean plate boundary interactions. *Nature* 2008, **456**(7221): 493-496.
- 362
- 363 16. Kröner A, Hoffmann JE, Xie HQ, Munker C, Hegner E, Wan YS, *et al.* Generation of
364 early Archaean grey gneisses through melting of older crust in the eastern Kaapvaal
365 craton, southern Africa. *Precambrian Research* 2014, **255**: 823-846.
- 366
- 367 17. Laurent O, Martin H, Moyen JF, Doucelance R. The diversity and evolution of late-
368 Archean granitoids: Evidence for the onset of "modern-style" plate tectonics between
369 3.0 and 2.5 Ga. *Lithos* 2014, **205**: 208-235.
- 370
- 371 18. Martin H, Moyen JF. Secular changes in tonalite-trondhjemite-granodiorite
372 composition as markers of the progressive cooling of Earth. *Geology* 2002, **30**(4): 319-
373 322.
- 374
- 375 19. Rosas JC, Korenaga J. Rapid crustal growth and efficient crustal recycling in the early
376 Earth: Implications for Hadean and Archean geodynamics. *Earth and Planetary
377 Science Letters* 2018, **494**: 42-49.
- 378
- 379 20. Bédard JH. A catalytic delamination-driven model for coupled genesis of Archaean
380 crust and sub-continental lithospheric mantle. *Geochimica Et Cosmochimica Acta*
381 2006, **70**(5): 1188-1214.
- 382
- 383 21. Gardiner NJ, Hickman AH, Kirkland CL, Lu YJ, Johnson T, Zhao JX. Processes of
384 crust formation in the early Earth imaged through Hf isotopes from the East Pilbara
385 Terrane. *Precambrian Research* 2017, **297**: 56-76.
- 386

- 387 22. Kamber BS. The evolving nature of terrestrial crust from the Hadean, through the
388 Archaean, into the Proterozoic. *Precambrian Research* 2015, **258**: 48-82.
389
- 390 23. Nebel O, Capitanio FA, Moyen JF, Weinberg RF, Clos F, Nebel-Jacobsen YJ, *et al.*
391 When crust comes of age: on the chemical evolution of Archaean, felsic continental
392 crust by crustal drip tectonics. *Philos T R Soc A* 2018, **376**(2132).
393
- 394 24. Rozel AB, Golabek GJ, Jain C, Tackley PJ, Gerya T. Continental crust formation on
395 early Earth controlled by intrusive magmatism. *Nature* 2017, **545**(7654): 332-+.
396
- 397 25. Sizova E, Gerya T, Stuwe K, Brown M. Generation of felsic crust in the Archean: A
398 geodynamic modeling perspective. *Precambrian Research* 2015, **271**: 198-224.
399
- 400 26. Smithies RH, Champion DC, Van Kranendonk MJ. Formation of Paleoproterozoic
401 continental crust through infracrustal melting of enriched basalt. *Earth and Planetary
402 Science Letters* 2009, **281**(3-4): 298-306.
403
- 404 27. Smithies RH, Lu YJ, Johnson TE, Kirkland CL, Cassidy KF, Champion DC, *et al.* No
405 evidence for high-pressure melting of Earth's crust in the Archean. *Nat Commun* 2019,
406 **10**.
407
- 408 28. Van Kranendonk MJ, Smithies RH, Griffin WL, Huston DL, Hickman AH, Champion
409 DC, *et al.* Making it thick: a volcanic plateau origin of Palaeoproterozoic continental
410 lithosphere of the Pilbara and Kaapvaal cratons. *Geol Soc Lond Spec Publ* 2015, **389**:
411 83-111.
412
- 413 29. Capitanio FA, Nebel O, Cawood PA, Weinberg RF, Chowdhury P. Reconciling thermal
414 regimes and tectonics of the early Earth. *Geology* 2019, **47**(10): 923-927.
415
- 416 30. Cawood PA, Hawkesworth CJ, Pisarevsky SA, Dhuime B, Capitanio FA, Nebel O.
417 Geological archive of the onset of plate tectonics. *Philos T R Soc A* 2018, **376**(2132).
418
- 419 31. Chowdhury P, Chakraborty S, Gerya TV, Cawood PA, Capitanio FA. Peel-back
420 controlled lithospheric convergence explains the secular transitions in Archean
421 metamorphism and magmatism. *Earth and Planetary Science Letters* 2020, **538**.
422
- 423 32. Chowdhury P, Gerya T, Chakraborty S. Emergence of silicic continents as the lower
424 crust peels off on a hot plate-tectonic Earth. *Nat Geosci* 2017, **10**(9): 698-+.

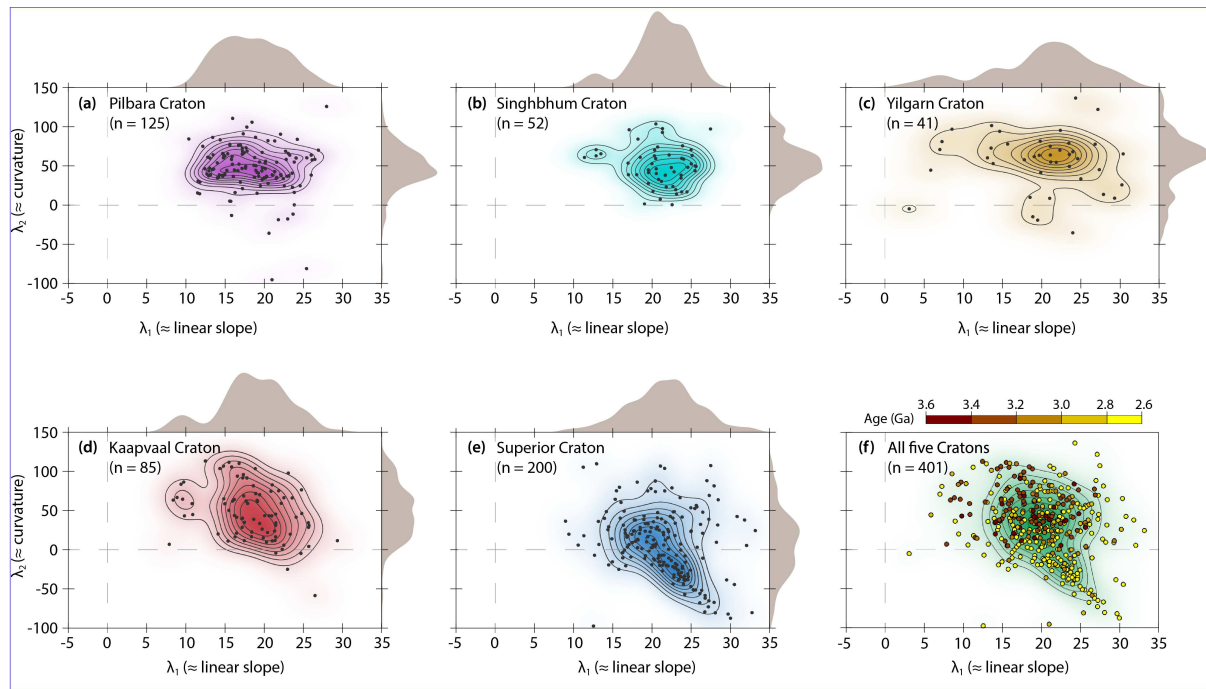
- 425
- 426 33. Moyen JF. The composite Archaean grey gneisses: Petrological significance, and
427 evidence for a non-unique tectonic setting for Archaean crustal growth. *Lithos* 2011,
428 **123**(1-4): 21-36.
- 429
- 430 34. Johnson IE, Kirkland CL, Gardiner NJ, Brown M, Smithies RH, Santosh M. Secular
431 change in TTG compositions: Implications for the evolution of Archaean geodynamics.
432 *Earth and Planetary Science Letters* 2019, **505**: 65-75.
- 433
- 434 35. O'Neill HS. The Smoothness and Shapes of Chondrite-normalized Rare Earth Element
435 Patterns in Basalts. *Journal of Petrology* 2016, **57**(8): 1463-1508.
- 436
- 437 36. Condie K. *Archean Greenstone belts*. Elsevier, 1981.
- 438
- 439 37. Guitreau M, Blichert-Toft J, Martin H, Mojzsis SJ, Albarede F. Hafnium isotope
440 evidence from Archean granitic rocks for deep-mantle origin of continental crust. *Earth
441 and Planetary Science Letters* 2012, **337**: 211-223.
- 442
- 443 38. Martin H, Moyen JF, Guitreau M, Blichert-Toft J, Le Pennec JL. Why Archaean TTG
444 cannot be generated by MORB melting in subduction zones. *Lithos* 2014, **198**: 1-13.
- 445
- 446 39. Kendrick J, Yakymchuk C. Garnet fractionation, progressive melt loss and bulk
447 composition variations in anatectic metabasites: Complications for interpreting the
448 geodynamic significance of TTGs. *Geosci Front* 2020, **11**(3): 745-763.
- 449
- 450 40. Nandedkar RH, Hurlimann N, Ulmer P, Muntener O. Amphibole-melt trace element
451 partitioning of fractionating calc-alkaline magmas in the lower crust: an experimental
452 study. *Contrib Mineral Petr* 2016, **171**(8-9).
- 453
- 454 41. Shimizu K, Liang Y, Sun CG, Jackson CRM, Saal AE. Parameterized lattice strain
455 models for REE partitioning between amphibole and silicate melt. *Am Mineral* 2017,
456 **102**(11): 2254-2267.
- 457
- 458 42. Tiepolo M, Oberti R, Zanetti A, Vannucci R, Foley SF. Trace-element partitioning
459 between amphibole and silicate melt. *Rev Mineral Geochem* 2007, **67**: 417-451.
- 460
- 461 43. Herzberg C, Condie K, Korenaga J. Thermal history of the Earth and its petrological
462 expression. *Earth and Planetary Science Letters* 2010, **292**(1-2): 79-88.

- 463
- 464 44. Fischer R, Gerya T. Early Earth plume-lid tectonics: A high-resolution 3D numerical
465 modelling approach. *J Geodyn* 2016, **100**: 198-214.
- 466
- 467 45. Jain C, Rozel AB, Tackley PJ, Sanan P, Gerya TV. Growing primordial continental
468 crust self-consistently in global mantle convection models. *Gondwana Res* 2019, **73**:
469 96-122.
- 470
- 471 46. O'Neill C, Debaille V. The evolution of Hadean-Eoarchean geodynamics. *Earth and*
472 *Planetary Science Letters* 2014, **406**: 49-58.
- 473
- 474 47. Dey S, Mitra A, Nandy J, Mondal S, Topno A, Liu Y, *et al.* Early Crustal Evolution as
475 Recorded in the Granitoids of the Singhbhum and Western Dharwar Cratons. *Earth's*
476 *Oldest Rocks*. Elsevier, 2019, pp 741–792.
- 477
- 478 48. Cawood PA, Hawkesworth CJ. Continental crustal volume, thickness and area, and
479 their geodynamic implications. *Gondwana Res* 2019, **66**: 116-125.
- 480
- 481 49. Dhuime B, Wuestefeld A, Hawkesworth CJ. Emergence of modern continental crust
482 about 3 billion years ago. *Nat Geosci* 2015, **8**: 552–555(2015).
- 483
- 484 50. Weller OM, Copley A, Miller WGR, Palin RM, Dyck B. The relationship between
485 mantle potential temperature and oceanic lithosphere buoyancy. *Earth and Planetary*
486 *Science Letters* 2019, **518**: 86-99.
- 487
- 488 51. Brown M, Johnson T, Gardiner NJ. Plate Tectonics and the Archean Earth. *Annual*
489 *Review of Earth and Planetary Sciences* 2020, **48**.
- 490
- 491 52. Van Kranendonk MJ. Two types of Archean continental crust: Plume and plate
492 tectonics on early Earth. *Am J Sci* 2010, **310**: 1187–1209.
- 493
- 494 53. Palme H, O'Neill H. Cosmochemical estimates of mantle composition. . In: Carlson
495 RW (ed). *Treatise on Geochemistry*, 2nd Edition edn, vol. 3. Elsevier, 2014, pp 1–39.
- 496
- 497



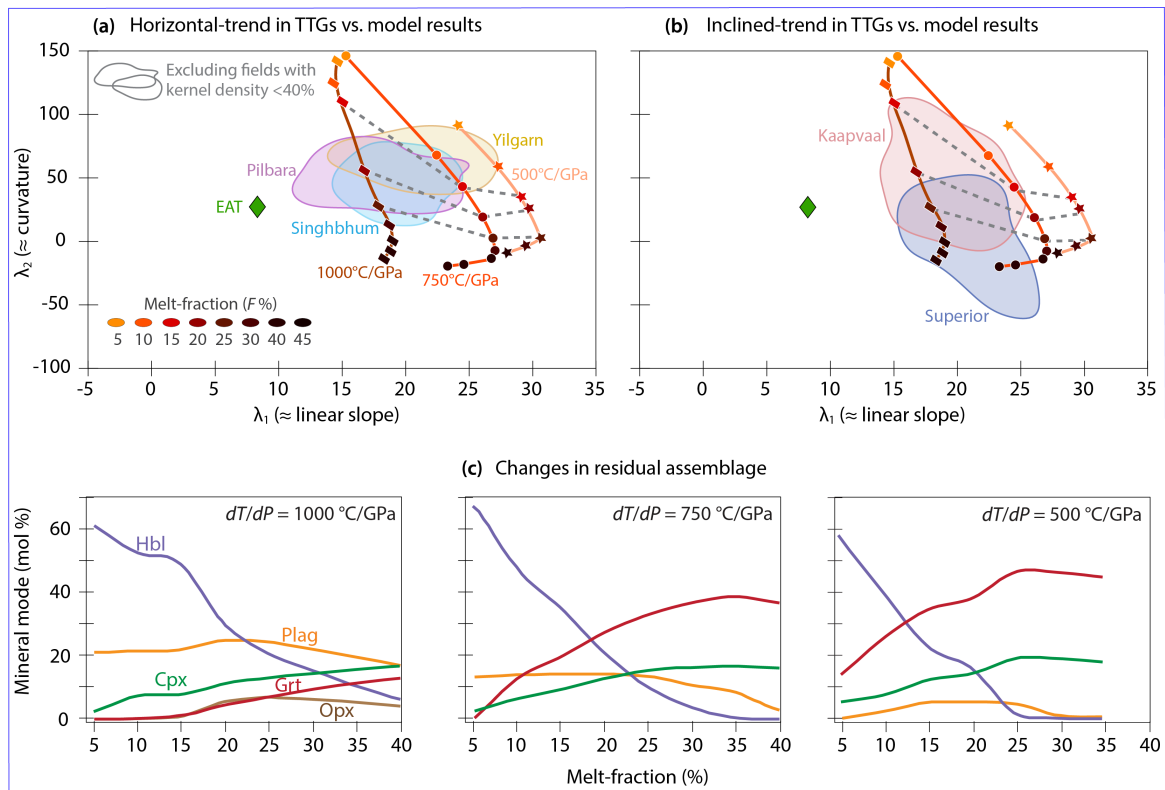
499

500 **Figure 1:** (a) Chondrite-normalized⁵³ rare-earth elements (REE) patterns of Archaean TTGs
 501 from Pilbara, Kaapvaal, Singhbhum, Yilgarn and Superior cratons (See Supplementary Table
 502 1). Note the near complete overlap among the datasets of different cratons. (b) A representative
 503 diagram showing the relation between REE_N pattern shapes and their corresponding positions
 504 in λ_1 vs. λ_2 space modified after³⁵.



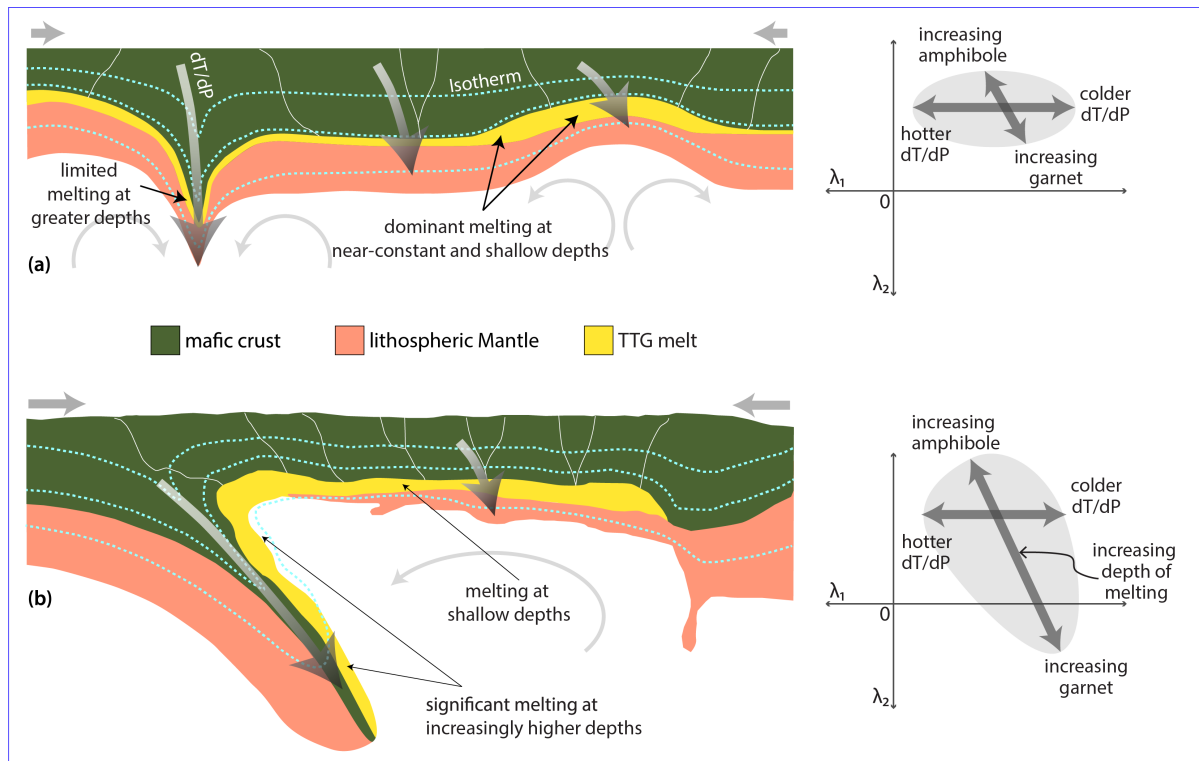
505

506 **Figure 2: (a-e)** Distribution (the black dots) of the REE_N patterns of Archaean TTGs from the
 507 Pilbara, Kaapvaal, Singhbhum, Yilgarn and Superior cratons (See Supplementary Table 1) in
 508 the λ -diagram space. Superimposed on them are the corresponding smoothed kernel density
 509 estimates (KDE; 2D coloured fields) and their contours (excluding the 10% outliers). Note the
 510 distinct horizontal-trend for the upper three cratons and the inclined-trend for the lower two
 511 cratons (see text). Individual (1D-) KDEs of λ_1 and λ_2 parameters are also presented along the
 512 top and right-hand axes, respectively to elucidate their variations among the studied cratons.
 513 Note that the spread in KDE of λ_1 are similar for all the five cratons, while that of λ_2 show
 514 contrasting features (sharp peaks for Pilbara, Singhbhum and Yilgarn TTGs versus broader
 515 flatter peaks for Kaapvaal and Superior TTGs). **(f)** A combined plot of the REE_N patterns of
 516 TTGs from all the five studied cratons The KDE field and its contours (excluding the 10%
 517 outlier) are also shown. Individual data points are colour-coded based on their crystallization
 518 ages. Note that the REE composition of Neoproterozoic TTGs of the Superior craton controls the
 519 inclined-trend of the combined dataset. See Supplementary Table 1 for the datasets.



520

521 **Figure 3: (a-b)** Plots of the REE_N patterns of modelled TTG-melts at different melt-fractions
 522 in λ -diagram. The TTG-melt compositions are calculated for the melting of enriched Archaean
 523 tholeiites (EAT³⁶) along three apparent geotherms (500, 750 and 1000°C/GPa). The KDE
 524 fields (excluding the <40% outliers) for natural TTG compositions from the five cratons are
 525 given for comparison. Note that the ‘horizontal-trend’ (a) corresponds to different melt-
 526 fractions formed along different apparent geotherms as shown by the dashed black lines,
 527 whereas the ‘inclined-trend’ (b) is produced by the different melt-fractions forming along the
 528 apparent geotherms. (c) Plots showing the abundances of dominant residual minerals at
 529 different modelled melt-fractions for each of the apparent geotherm considered for melting
 530 modified after Kendrick and Yakymchuk³⁹; see text for details. Note that the modelled TTG-
 531 melts evolve towards $-\lambda_2$ values with increasing melt-fraction for any apparent geotherm,
 532 concurrently with an increasing garnet-to-amphibole ratio. Mineral abbreviations: Grt- garnet;
 533 Hbl- hornblende; Plag- plagioclase; Cpx- clinopyroxene; Opx- orthopyroxene.



534

535 **Figure 4: (a)** Schematic diagrams of mafic crustal melting at the base of a thickened crust²⁵
 536 and within a peel-back controlled convergent setting^{31, 32} showing their correlation with the
 537 observed REE compositional trends in λ -diagram. The horizontal spread in λ_1 values,
 538 representing melting along different apparent geotherm at shallower depths, is reconciled by
 539 melting: above the mantle upwelling (hot dT/dP ; dT/dP represents apparent geotherm); at the
 540 base of thickened crust (intermediate dT/dP); and within the crustal drips (relatively, colder
 541 dT/dP). **(b)** In contrast, lithospheric peeling causes melting within delaminating crust and at
 542 the base of a thinned, crust formed in front of it. The former melting site reconciles with the
 543 progressive melting of mafic crust along a narrow range of apparent geotherms and thereby,
 544 explains the variation in λ_2 values while the later melting site can account for the spread in λ_1
 545 values.

546 **Supplementary Figures and Tables**

547 **Supplementary Figure 1:** Plots of the CI-normalized REE compositions of the TTGs from five
548 different cratons.

549 **Supplementary Figure 2:** Modelling the partitioning of REEs in felsic melts derived from
550 enriched Archaean tholeiites (EAT).

551 **Supplementary Figure 3:** Modelling the partitioning of REEs in felsic melts derived from
552 depleted Archaean tholeiites (DAT).

553 **Supplementary Figure 4:** Modelling the partitioning of REEs in felsic melts derived from the
554 enriched Coucal basalts.

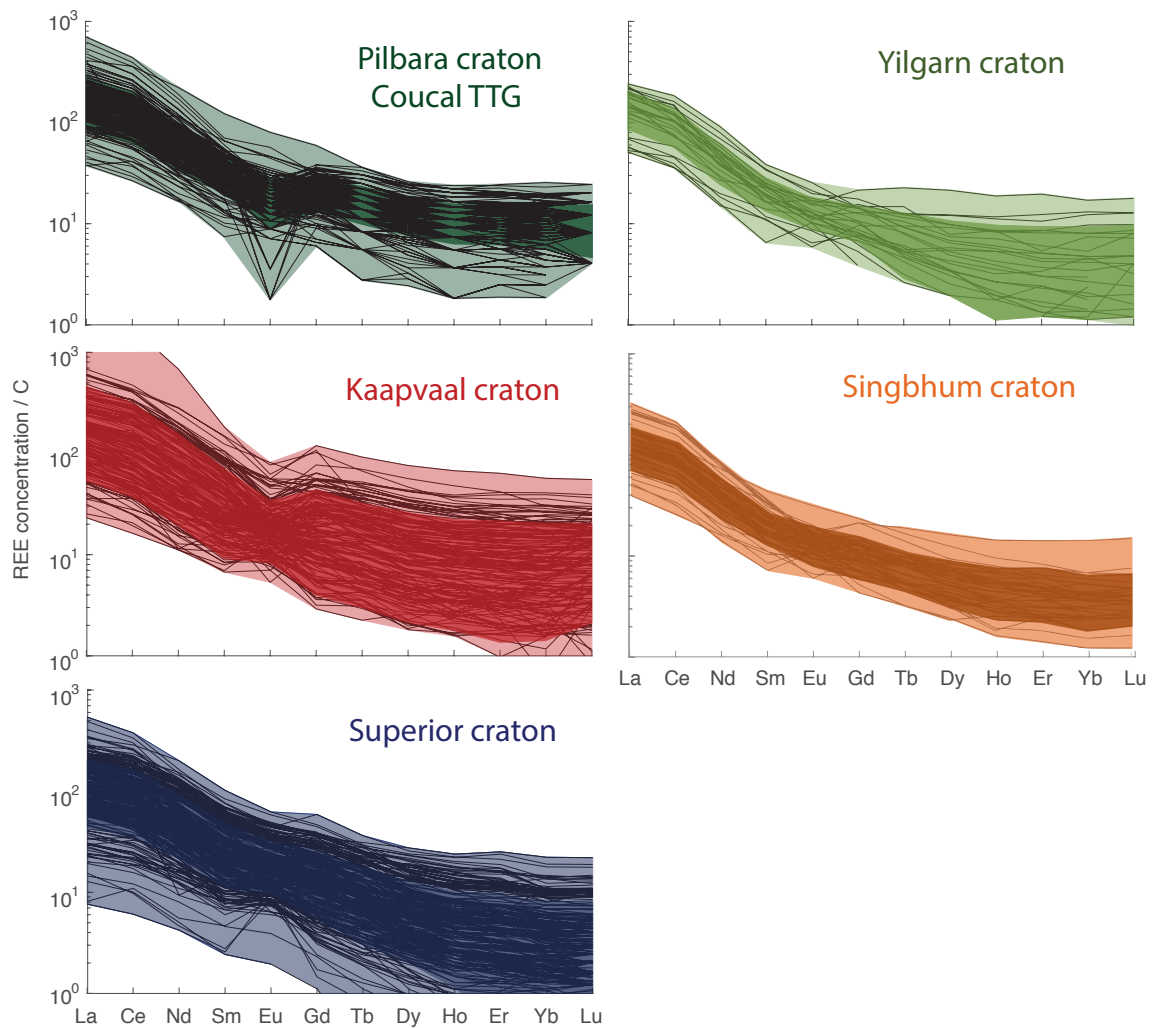
555 **Supplementary Table 1:** The REE composition of TTGs from all the studied cratons.

556 **Supplementary Table 2:** List of the K_d values used in the trace element modelling.

557 **Supplementary Table 3:** Compositions for the average EAT, DAT and Coucal Basalt.

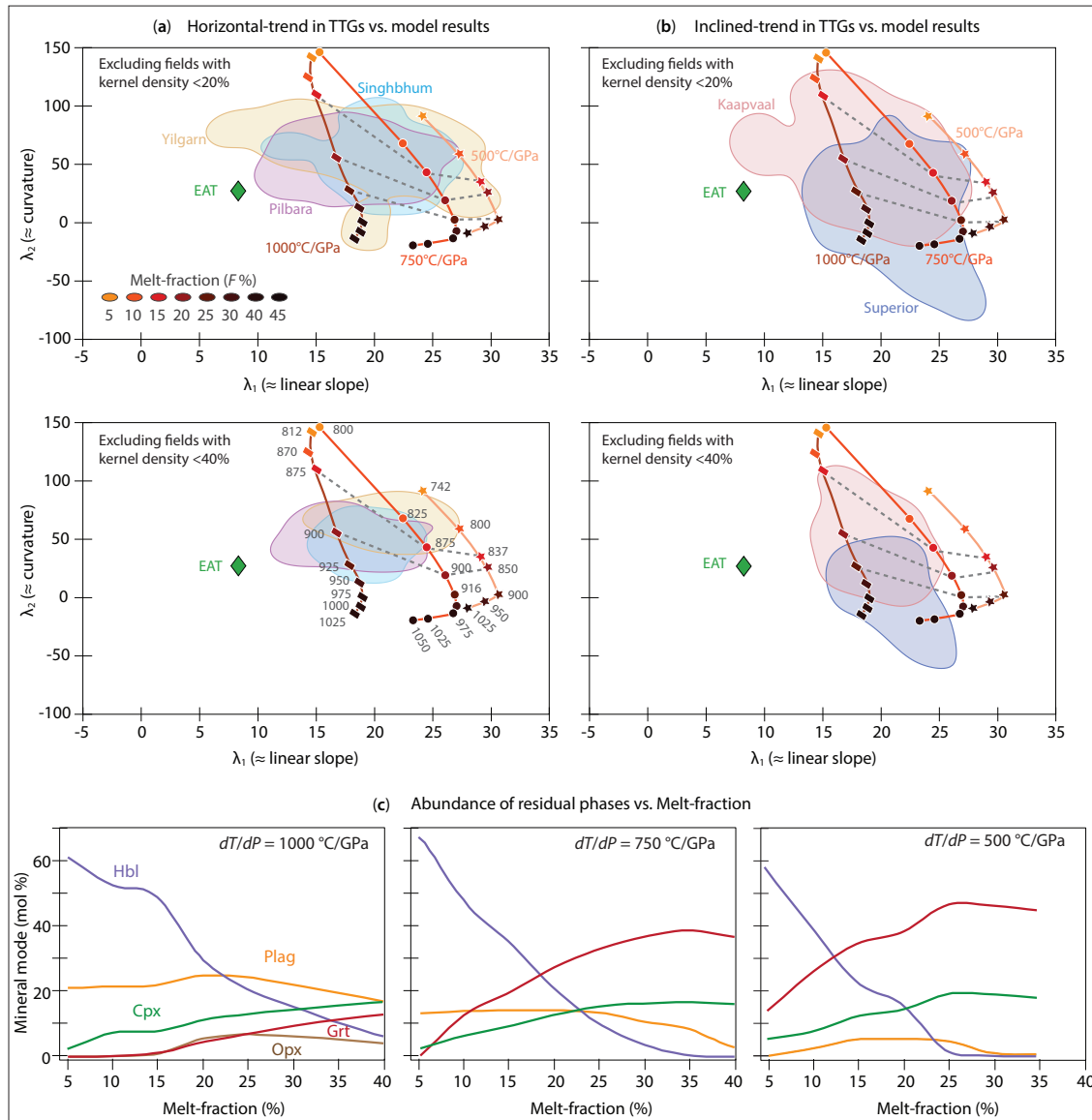
558 **Supplementary Table 4:** REE compositions of the modelled melts obtained from with EAT
559 and DAT source rock compositions.

560 **Supplementary Table 5:** REE composition of the modelled melts derived from the average
561 Coucal basalt composition.



563

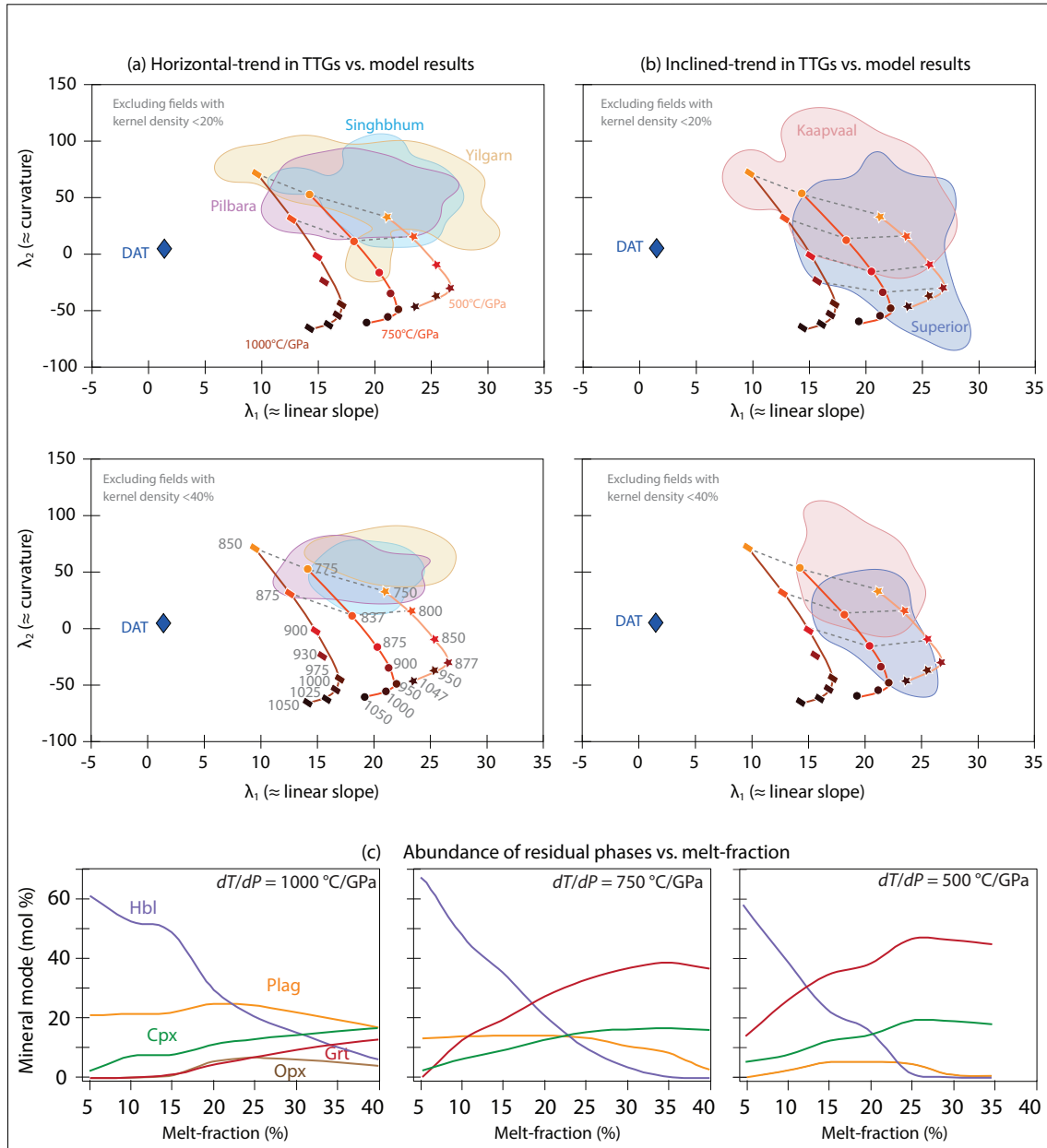
564 **Supplementary Figure 1: Plots of the CI-normalized REE compositions of the TTGs from**
 565 **five different cratons.** The dark-shaded areas represent 80% of dataset for each craton and
 566 thus, represents their dominant compositional ranges. See Figure 1 for the comparison among
 567 these REE Patterns of different cratons. The data used for this plot are given in Supplementary
 568 Table 1.



569

570 **Supplementary Figure 2: Modelling the partitioning of REEs in felsic melts derived from**
 571 **enriched Archaean tholeiites (EAT).** (a-b) Melting of the average EAT composition ^{36, 39}
 572 along three different apparent geothermal gradients (500, 750 and 1000°C/GPa) is considered.
 573 The coloured fields represent the composition of TTGs from different cratons. TTGs with
 574 horizontal trends show a good correlation with the higher melt-fractions (~15-25%) of the
 575 modelled melts irrespective of the geotherms, whereas the TTGs defining the inclined trends
 576 are best represented by the melt-fractions varying between >10-40% that formed along the

577 geotherm of $>750\text{-}1000^\circ\text{C/GPa}$. **(c)** Plots of the modal abundances of residual phases as a
578 function of melt-fraction for different geotherms of melting³⁹.



579

580 **Supplementary Figure 3: Modelling the partitioning of REEs in felsic melts derived from**

581 **depleted Archaean tholeiites (DAT).** (a-b) Melting of the average DAT composition^{36, 39}

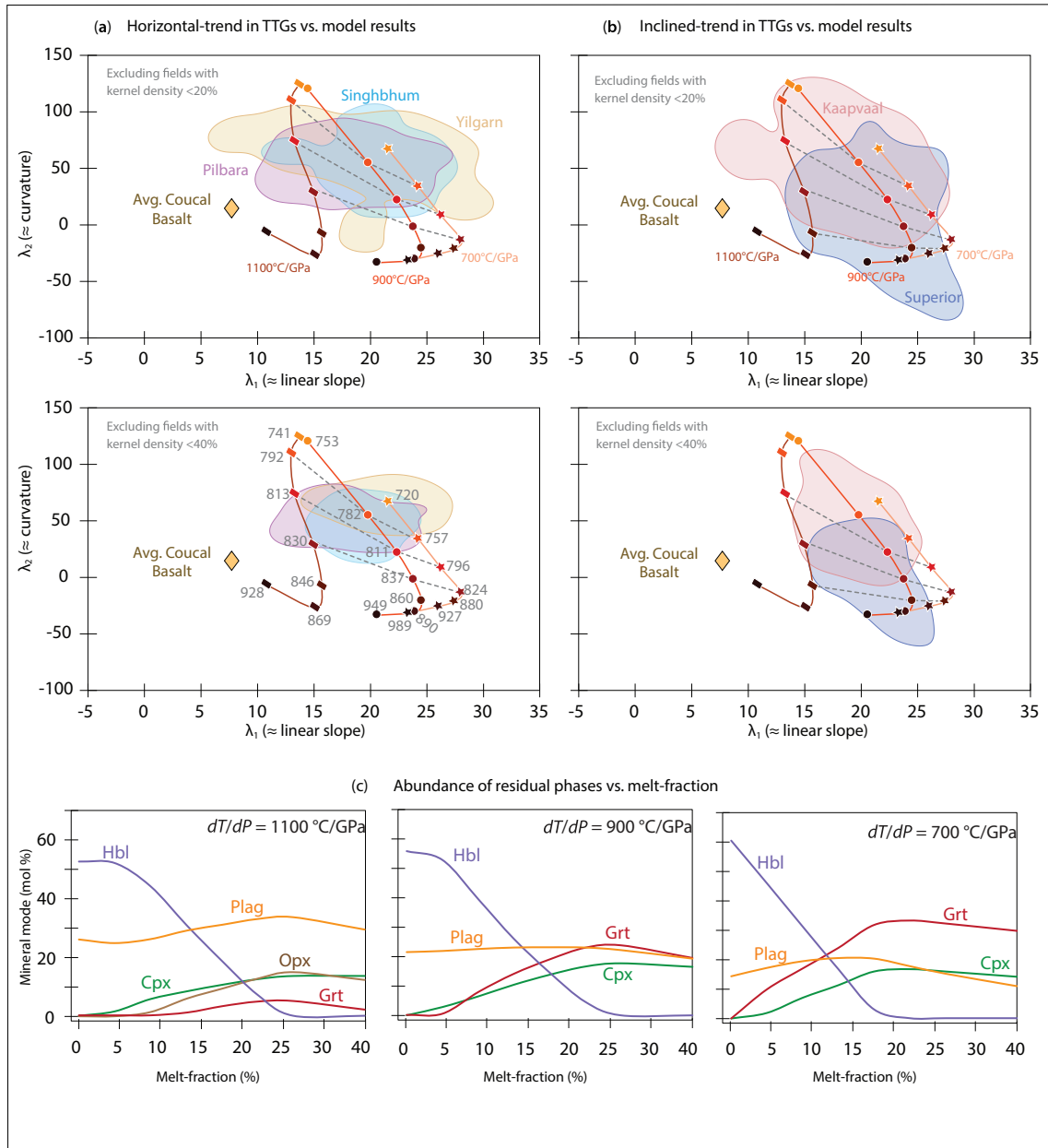
582 along three different apparent geothermal gradients (500, 750 and 1000°C/GPa) is considered.

583 The coloured fields represent the composition of TTGs from different cratons. Only the low

584 melt-fractions (5-10 %) formed along the colder geotherms (500-750°C/GPa) can reconcile the

585 composition of natural TTGs (except for the Superior Province). However, such low melt-

586 fractions cannot match the major element compositions of TTGs^{5, 8, 10}. The Superior Province
587 TTGs, however, show a good resemblance with the compositions of higher melt-fractions
588 (~15-25%) formed along the geotherms of 500-750°C/GPa, suggesting DAT could be their
589 source rock. **(c)** Plots of the modal abundances of residual phases vs. melt-fraction for different
590 melting geotherms³⁹.



591

592 **Supplementary Figure 4: Modelling the partitioning of REEs in felsic melts derived from**

593 **the enriched Coucal basalts.** Melting of the average Coucal basalt composition⁸ along three

594 different apparent geothermal gradients (700, 900 and 1100°C/GPa) is considered. The REE

595 composition of the higher melt-fraction (>15-25%) formed along hotter geotherms (900-

596 1100°C/GPa) agrees well to those of the natural TTGs at higher melt-fractions. The results are

597 consistent with the findings of Johnson et al. (2017)⁸.

Figures

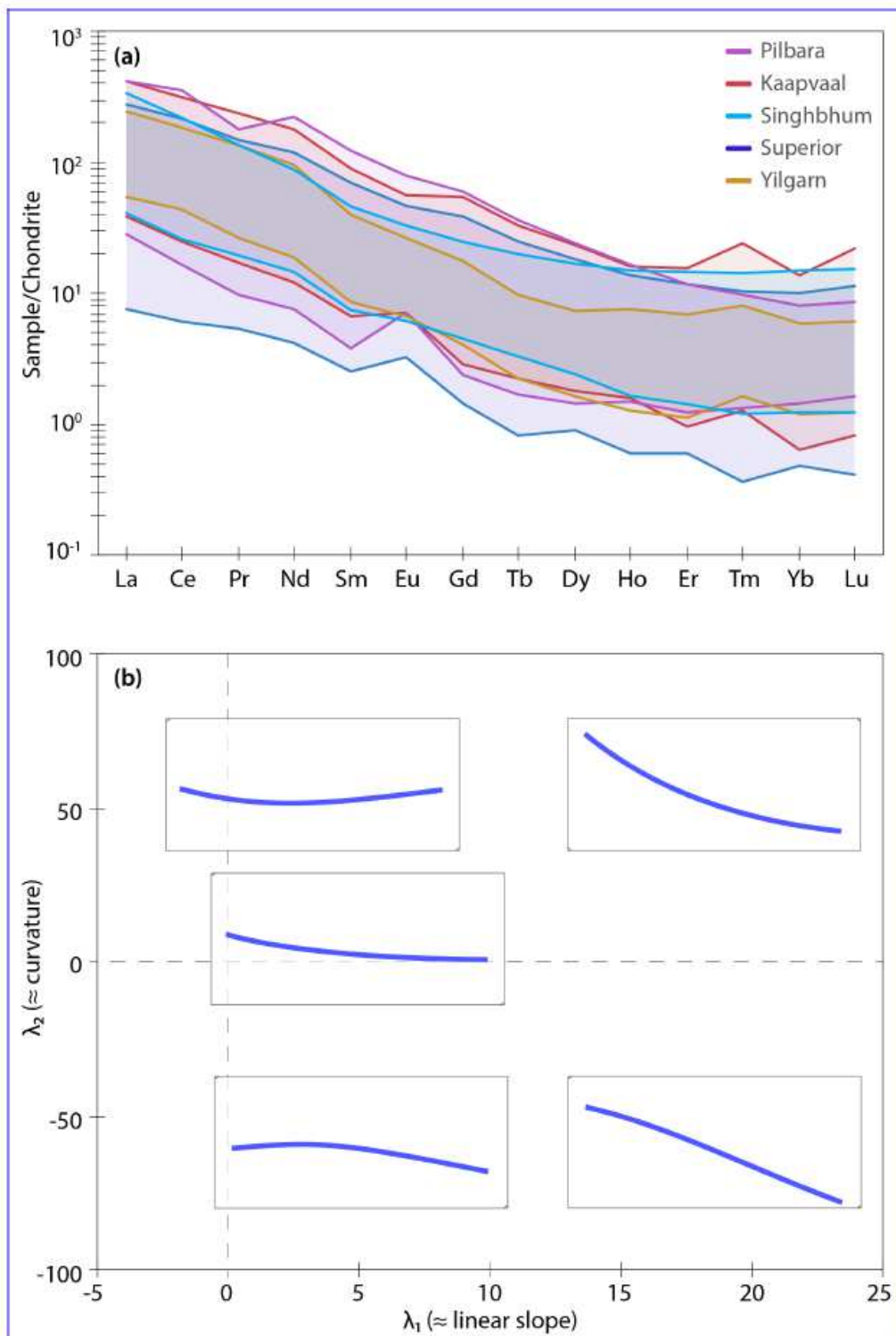


Figure 1

(a) Chondrite-normalized REE patterns of Archaean TTGs from Pilbara, Kaapvaal, Singhbhum, Yilgarn and Superior cratons (See Supplementary Table 1). Note the near complete overlap

among the datasets of different cratons. (b) A representative diagram showing the relation between REEN pattern shapes and their corresponding positions in λ_1 vs. λ_2 space modified after 35.

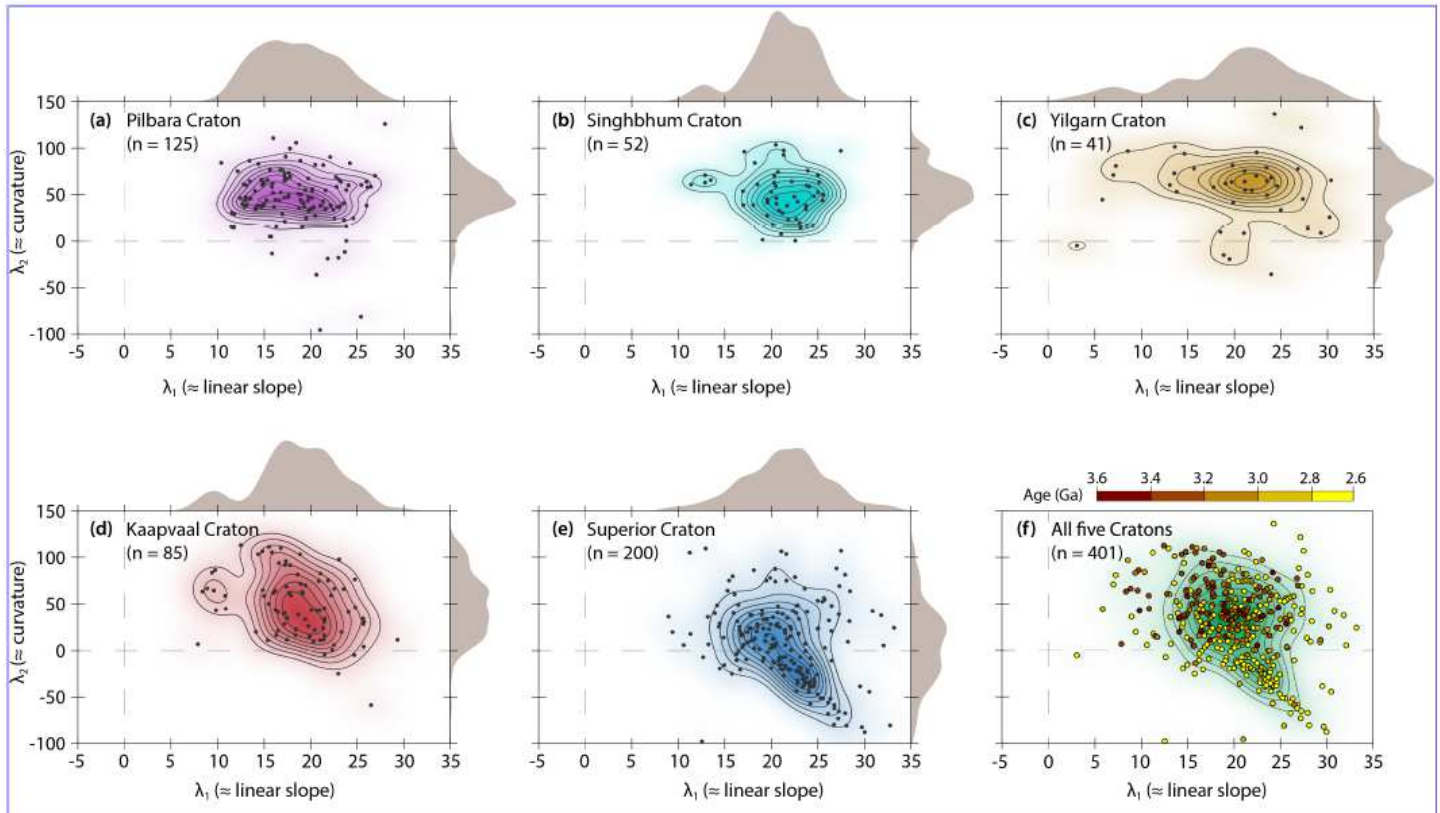


Figure 2

(a-e) Distribution (the black dots) of the REEN patterns of Archaean TTGs from the Pilbara, Kaapvaal, Singhbhum, Yilgarn and Superior cratons (See Supplementary Table 1) in the λ -diagram space. Superimposed on them are the corresponding smoothed kernel density estimates (KDE; 2D coloured fields) and their contours (excluding the 10% outliers). Note the distinct horizontal-trend for the upper three cratons and the inclined-trend for the lower two cratons (see text). Individual (1D-) KDEs of λ_1 and λ_2 parameters are also presented along the top and right-hand axes, respectively to elucidate their variations among the studied cratons. Note that the spread in KDE of λ_1 are similar for all the five cratons, while that of λ_2 show contrasting features (sharp peaks for Pilbara, Singhbhum and Yilgarn TTGs versus broader flatter peaks for Kaapvaal and Superior TTGs). (f) A combined plot of the REEN patterns of TTGs from all the five studied cratons. The KDE field and its contours (excluding the 10% outlier) are also shown. Individual data points are colour-coded based on their crystallization ages. Note that the REE composition of Neoproterozoic TTGs of the Superior craton controls the inclined-trend of the combined dataset. See Supplementary Table 1 for the datasets.

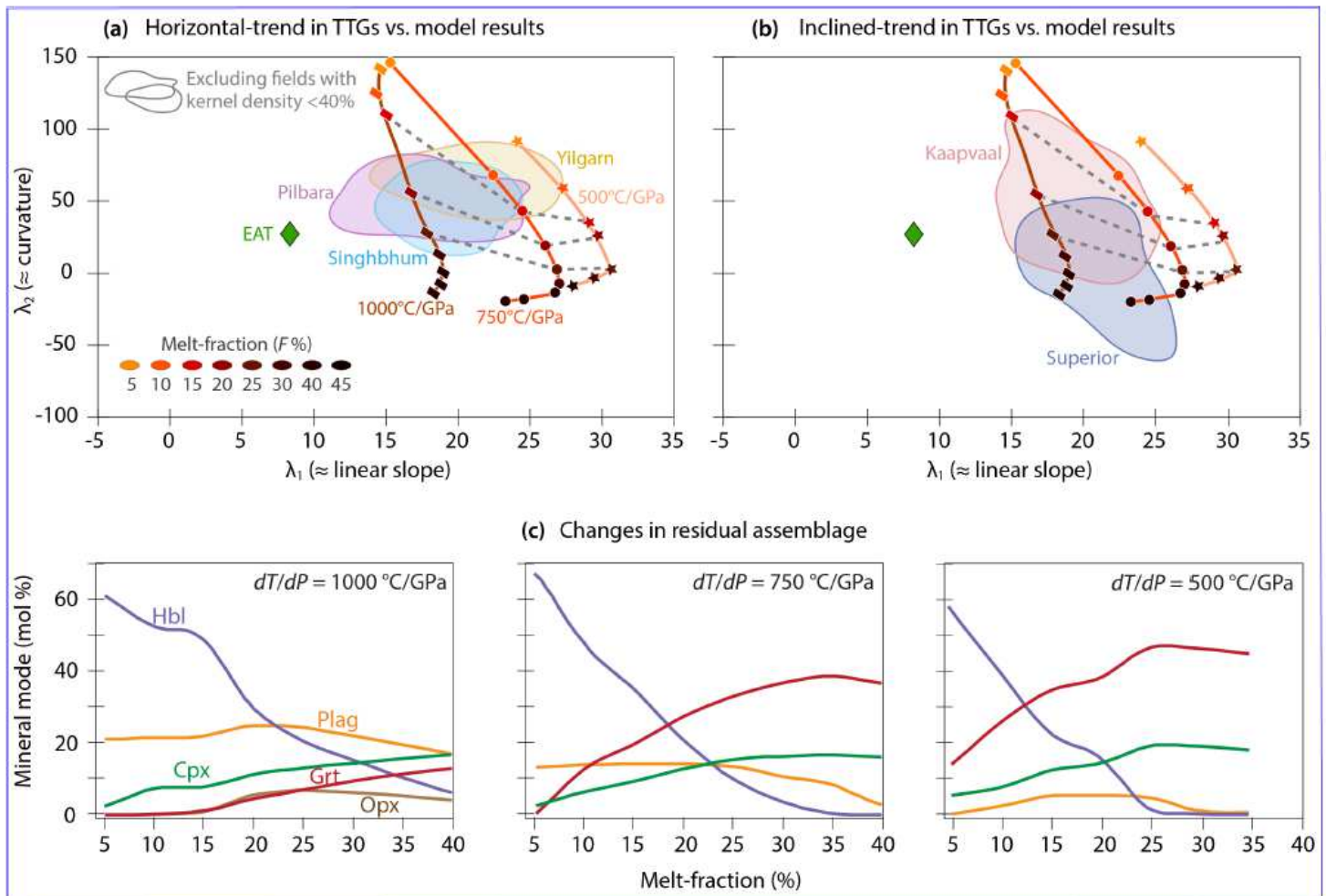


Figure 3

(a-b) Plots of the REEN patterns of modelled TTG-melts at different melt-fractions in λ -diagram. The TTG-melt compositions are calculated for the melting of enriched Archaean tholeiites (EAT 36) along three apparent geotherms (500, 750 and 1000°C/GPa). The KDE fields (excluding the <40% outliers) for natural TTG compositions from the five cratons are given for comparison. Note that the ‘horizontal-trend’ (a) corresponds to different melt-fractions formed along different apparent geotherms as shown by the dashed black lines, whereas the ‘inclined-trend’ (b) is produced by the different melt-fractions forming along the apparent geotherms. (c) Plots showing the abundances of dominant residual minerals at different modelled melt-fractions for each of the apparent geotherm considered for melting modified after Kendrick and Yakymchuk 39; see text for details. Note that the modelled TTG-melts evolve towards $-\lambda_2$ values with increasing melt-fraction for any apparent geotherm, concurrently with an increasing garnet-to-amphibole ratio. Mineral abbreviations: Grt- garnet; Hbl- hornblende; Plag- plagioclase; Cpx- clinopyroxene; Opx- orthopyroxene.

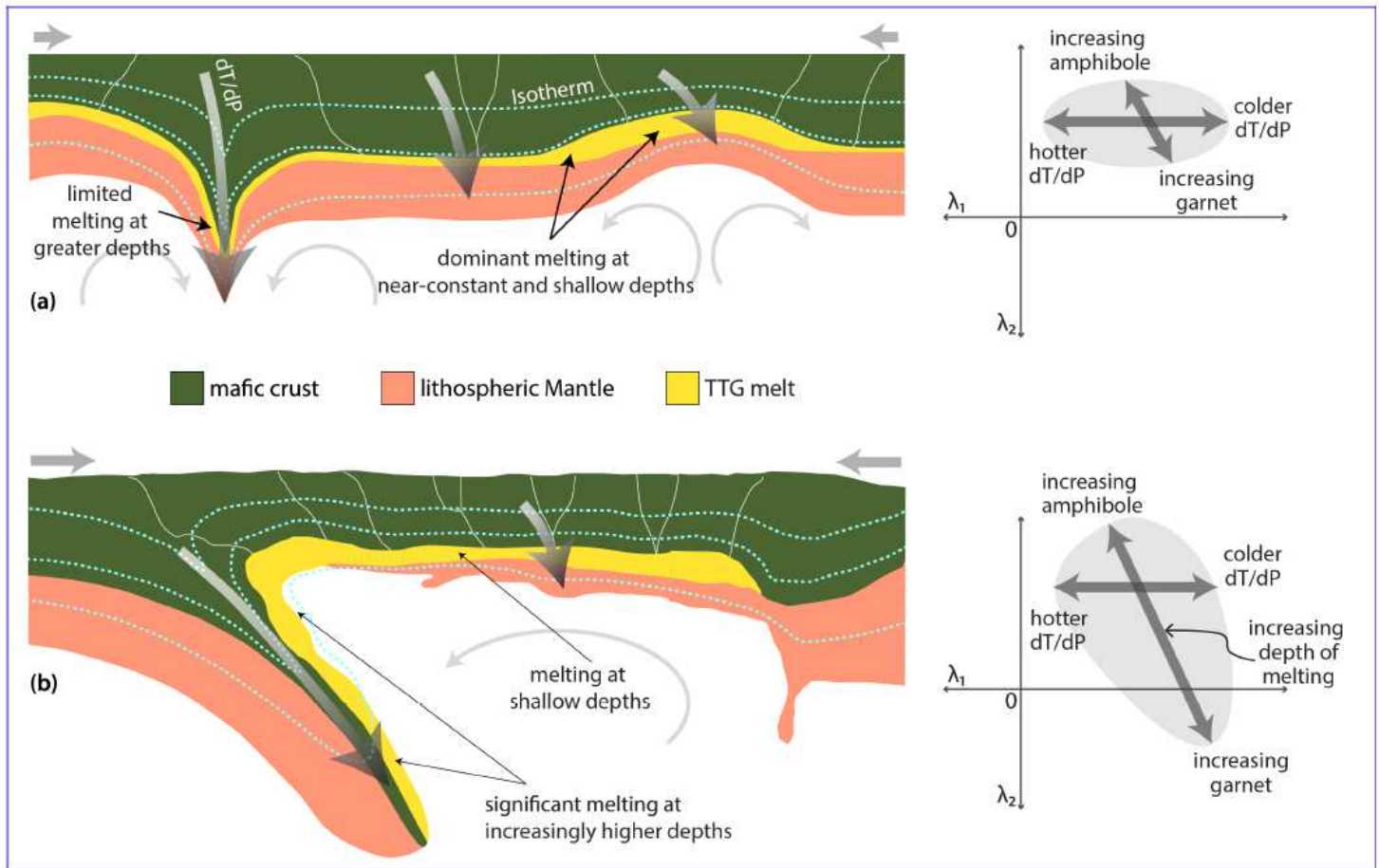


Figure 4

(a) Schematic diagrams of mafic crustal melting at the base of a thickened crust 25 and within a peel-back controlled convergent setting 31, 32 showing their correlation with the observed REE compositional trends in λ -diagram. The horizontal spread in λ_1 values, representing melting along different apparent geotherm at shallower depths, is reconciled by melting: above the mantle upwelling (hot dT/dP ; dT/dP represents apparent geotherm); at the base of thickened crust (intermediate dT/dP); and within the crustal drips (relatively, colder dT/dP). (b) In contrast, lithospheric peeling causes melting within delaminating crust and at the base of a thinned, crust formed in front of it. The former melting site reconciles with the progressive melting of mafic crust along a narrow range of apparent geotherms and thereby, explains the variation in λ_2 values while the later melting site can account for the spread in λ_1 values.

Supplementary Files

This is a list of supplementary files associated with this preprint. Click to download.

- [SupplementaryTables.xlsx](#)
- [SupplementalFigures.pdf](#)